nature research

https://doi.org/10.1038/s41565-020-0754-x

Supplementary information

High quality factor phase gradient metasurfaces

In the format provided by the authors and unedited

Supplementary Materials - High Quality Factor Phase Gradient Metasurfaces

Mark Lawrence,[1†*] David R. Barton III,[1†*] Jefferson Dixon,[2] Jung-Hwan Song,[3] Jorik van de Groep,[3,5] Mark L. Brongersma,[3] Jennifer A. Dionne[1,4†]

[1]*Department of Materials Science and Engineering, Stanford University, Stanford, CA, USA*

[2]*Department of Mechanical Engineering, Stanford University, Stanford, CA, USA*

[3]*Geballe Laboratory for Advanced Materials, Stanford University, Stanford, CA, USA*

[4]*Department of Radiology, Stanford University, Stanford, CA, USA*

[5]*Present address: Van der Waals-Zeeman Institute for Experimental Physics, Institute of Physics, University of Amsterdam, Amsterdam, Netherlands.*

[†]*To whom correspondence should be addressed; E-mail: markl89@stanford.edu, dbarton@stanford.edu, jdionne@stanford.edu.*

[*]*These authors contributed equally to this work*

1. Phase gradient metasurface design

For full 2π phase control while maintaining high transmittance, we designed silicon nanostructures that act as a Huygens metasurfaces by spectrally overlapping the electric and magnetic dipoles. The evolution from separate to overlapping resonances can be seen in supplementary Fig. S1 which plots the transmission spectra through nano-bar arrays with heights varying from 450 to 600 nm. When the bars are 450 nm tall, two distinct resonances appear near 1270 nm and 1400 nm. Corresponding field plots on the right demonstrate that these resonances are electric and magnetic dipole-like in character. While geometrically tunable, these modes show very low transmission. As the height is increased, there is spectral overlap of the dipole modes. Near 600 nm, the overlap is sufficient to increase the transmittance substantially. Varying the widths of the 600 nm tall bars then modulates the outgoing phase while the

transmittance remains very high. This is exemplified by the broad wavelength range over which the beamsteering response is efficient. We numerically vary the nanobar width and confirm the high amplitude and full phase response at two different wavelengths spaced by 100 nm (1400 nm and 1500 nm, Fig. S2). From supplementary Fig. S2 we pick three elements with phase delays differing by $2\pi/3$, used in Figs. 1 and 2 of the main text. To visualize the phase gradient response, supplementary Fig. S3 compares the electric field associated with the three bars. With each element transmitting a similar amplitude but different phase, the exiting wave stays approximately planar but is bent to travel in a new direction dependent on the periodicity of the supercell. Note that each bar simulation is done independently; that is, each simulation assumes that there is infinite periodicity in the x direction of nanobars with the same width. Fig. S3 is presented for the purpose of visualization, all simulations in the main text take all diffraction effects into account.

2. High Q Beam-steering simulation details

With the chosen perturbation geometry, Fig. 1d of main text shows the theoretical diffraction efficiency through the metasurface, and a quality factor of ~8,000 is extracted from the data. We have replotted the relevant scattering into the 0^{th} and -1^{st} diffracted orders in supplementary Fig. S4 to more clearly show the lineshape. As seen, both orders show similar asymmetric spectral lineshapes. As mentioned in the main text, reducing the notch depth to 50 nm increases the quality factor from ~8,000 to approximately 39,000. We have reproduced the simulation and fit below in supplementary Fig. S5. We also note that the simulated $+1^{st}$ order transmittance still drops to 0. Our experimental measurements show less contrast, which we attribute to fabrication imperfections giving rise to scattering losses.

3. Finite size effects in the diffraction plane

From a naive interpretation of Fig. 1f of the main text, showing a significantly stronger nearfield enhancement within the notched nanoantenna at the GMR, one may conclude that close to the GMR the notched nanoantenna also dominates the scattering response. In fact, the nearfield map is a poor indicator of spatially dependent scattering strength. In Fig. S6, we show the numerically calculated total scattering cross section and corresponding nearfield enhancement for an isolated notched nanoantenna with dimensions corresponding to the largest bar in Fig. 1 of the main text. This structure can be seen to support three resonances, two of which represent high Q GMRs, shown in Fig. S6A-B, and one represents a low Q Mie resonance, shown in Fig. S6C. By comparing the three modes we can clearly see that dramatically different field enhancements occur, depending on the type and linewidth of the mode being considered. In all cases, the scattering cross section also increases considerably on resonance. However, the peak amplitude of the scattering cross section remains similar for all modes. Not only is there not a strong correlation between peak field enhancement and peak scattering strength, but the mode exhibiting the highest field enhancement, Fig. S6A, actually shows the weakest peak scattering strength. This analysis justifies treating the low Q and high Q resonances of our nanoantennas on equal footing when engineering the farfield scattering of our phase gradient metasurface. Thus, the elements introduced in the present study can be used as generalizable metasurface elements and contribute similarly to other elements, regardless of the high-Q modulation.

This is also conceptually supported by the results presented in Fig. 3 of the main text. If the perturbed metasurface elements scattered substantially stronger than the unperturbed neighboring bars, then on resonance one would expect the scattering response to look like a symmetric diffraction grating. However, we do not observe this either experimentally or theoretically. Fig.

3 of the main text demonstrates that we can design a high-Q metasurface which exhibits beamsteering only on resonance, which necessarily requires the scattering from neighboring bars to be comparable in strength. Further, we can design beamsteering metasurfaces with no significant changes to the scattering response on resonance (that is, Fig. 3b in the main text demonstrates that beamsteering can be maintained over its resonance), while the electric field enhancement can grow significantly.

We have also experimentally verified that the effects we observe arise due to a phase gradient metasurface, rather than traditional diffraction grating effects. While the current embodiment of our high-Q idea utilizes long (300 μm) bars to effectively couple light into the nanostructure, this is not a requirement. We can readily scale our metasurfaces down to a few μm on each side. For example, Fig S7 shows an SEM image of a fabricated beamsteering sample similar to that presented in the main text, where only 10 bars (3.33 unit cells) are used. The truncation in the phase gradient direction is unrelated to the resonant phenomena we observe experimentally, and we indeed observe that the high-Q resonance is unaffected by the finite size along the phase gradient direction. In order to scale the bar lengths down to μm size, a variety of techniques in the photonic crystal cavity community could be borrowed. For example, simple dielectric mirrors can be patterned at the ends of each bar which contains the guided mode resonance of interest. Photonic crystal mirrors can be designed extremely broadband (>100 nm) and with high reflectivity (>99%), such that the added reflection can be used to make a cavity within the metasurface element. In doing so, metasurfaces with total sizes on the order of μm with high quality factor resonances can be envisioned.

4. Dispersion of perturbed metasurface

Considering the waveguide mode dispersion for each bar, we selected perturbation dimensions commensurate with the wavelength of interest. While the perturbations are relatively small compared to the nanobar, for the larger notch depths, Bragg scattering nevertheless opens a bandgap in the dispersion, shifting the resonant wavelength from the simple momentum crossing in Fig. 1c of the main text. In Fig.1c of the main text we plot the guided mode dispersion for a phase gradient metasurface composed of continuous bars. We then argue that resonant modes in the far-field diffraction spectra of notched bars occur due to weak coupling between guided and freespace light. However, as we increase the notch depths we expect the notches to modify the guided mode dispersion as well as provide coupling to freespace. In Fig. S8 we explicitly calculate the dispersion for the notched nanoantenna used within our beam steering metasurfaces with increasing depth, d. Here we can see that in addition to decreasing the mode index, increasing d produces more Bragg scattering which opens a larger band gap at k=0. The wavelengths of our measured GMRs agree well with the k=0 crossings of the upper branches in S8.

5. Additional information for beam steering measurements

We additionally quantify the quality factors and resonant wavelengths for all parameter sweeps reported in main text Fig. 2. First, supplementary Fig. S9 plots the resonant wavelength as a function of notch depth in main text Fig. 2c (left panel) and the resonant wavelength as a function of perturbation period in main text Fig. 2e. A monotonic redshift in the resonant wavelength can be seen as the notch gets smaller, consistent with a decreased perturbation and increased average refractive index. Similarly, there is a monotonic redshift in the resonant wavelength as the perturbation period increases, commensurate with the guided mode dispersion presented in main text Fig. 1. Supplementary Fig. S10 plots the quality factor as a function of

perturbation period, experimental data is given in Fig. S10A and the corresponding simulated data is given in Fig. S10B. While there are discrepancies likely coming from irregularities in the pattern across the chip, both the experimental and simulated data show the highest Q for a 570 nm period.

Here, we briefly discuss a key difference between our guided mode resonant nanoantennas and whispering gallery resonators (WGRs). In the case of WGRs, as well as most other microcavities, resonant modes can be defined in the absence of a physical mechanism for coupling light in or out of the cavity. With a dielectric disk or ring of a particular radius r, for example, resonant feedback will occur whenever the optical wavelength matches an integer multiple of the circumference $2\pi r$. Continuous silicon nano-bars, on the other hand, support potential resonant modes formed by counter propagating guided solutions at all wavelengths. Unlike the dielectric disk or ring for which an evanescent or grating coupler needs to be carefully designed in order to efficiently excite the predefined resonant mode, a periodic perturbation applied to the nano-bar generates a series of resonant modes out of the continuous guiding spectrum. Therefore, the light coupled into the bar is automatically phase matched, leading to a critically coupled state as long as no scattering or absorption loss is present.

6. Modal symmetry considerations in high-Q nanoantennas

The spectral position of a guided mode resonance in a nanoantenna is mostly determined by the dispersion of modes guided along the structure and the perturbation period used to excite them. The spatial profile of the corresponding scattering, on the other hand, represents a richer parameter space. In Figs. 1 and 2 of the main text we focus mainly on a mode with horizontally polarized electric fields. Therefore, we should expect the resonant scattering to be dominated by an in-plane electric dipole. In Fig. S11 we solve for the eigenmodes of our GMR nanoantenna.

Indeed, we find an electric dipole emission pattern when notches are placed symmetrically on both sides of the structure. But when the inversion symmetry is broken by shifting the notched region to one side, the emission pattern clearly changes. The direction corresponding to the peak intensity can be seen to rotate away from the side with the deepest notch. This provides a geometrical degree of freedom for tuning the relative response of the various transmissive diffraction orders, as one should expect the GMR contrast to be maximal within a diffraction order aligned with its peak emission direction.

In Fig. 3 of the main text we show numerically that switching to a vertically polarized electric dipole GMR allows us to imbue a phase gradient metasurface with new spectral shapes, including narrowband and slow-light steering. In Fig. S12 we plot the eigenmode emission pattern of this mode. Unlike the in-plane dipole, we find that now the field pattern is symmetric about the vertical axis. Therefore, without any structural symmetry breaking, scattering into a vertically propagating plane wave is forbidden. We also now see that instead of a directional dependence in the emitted intensity, shifting the notched region alters the phase delay of radiation emitted to the left and right of the nanoantenna. This provides a way to tune the relative GMR lineshape in the different diffraction orders rather than the contrast. While we have focused here on electric dipoles, one could envision a host of high Q multipoles being possible in different dielectric structures.

7. Additional Beamsteering metasurfaces

The main text focuses on beamsteering metasurfaces which diffract light preferentially to +45 degrees. These samples used 3 metasurface bar elements with center-to-center spacings of 707 nm. We can easily change the phase gradient period and meta-element spacing to approximate other linear phase gradients. Fig. S13 shows this, where we have designed and

fabricated a variety of metasurface samples which send light to +36 degrees. This has a phase gradient unit cell of 2.5 μm, with center-to-center spacing of elements of 500 nm. Performing identical spectroscopic measurements as before, we see extremely efficient beamsteering (up to 80 percent) over almost 110 nm of bandwidth (Fig. S13A). Following the same prescription as before, we couple into GMRs specified by a perturbation period 550 nm and depth of 30 nm. A mode at around 1528 nm and Q exceeding 1500 can be observed for this metasurface.

In Fig. S13B, showing the effect of increasing the perturbation depth to 100 nm, we see a decrease in Q factor and an increase in resonant contrast, which can again be attributed to finite scattering loss. The GMR contrast is generally smaller in Fig. S13 than Fig. 2 of the main text, indicating a reduced overlap between the guided wave, the excitation wave, and the +1st diffracted wave. This problem could be remedied by carefully engineering the scattering profile of the GMR or combining multiple GMRs. For the larger perturbation depths additional modes also show up around 1480 nm. With the increased number of metasurface elements in the unit cell of the five bar device, these likely arise from nearfield coupling to neighboring bars. The mode coupling is noticeable when the perturbation depth is 70 nm, but is markedly enhanced at d = 100 nm, where the main waveguided mode is more spectrally overlapped with the additional modes. To confirm our hypothesis, we fabricated samples where the perturbations are on either the left or right side of the largest bar in each unit cell. The spectra are shown in Fig. S13C. When the perturbation is on the left side, we see efficient coupling to one mode near 1520 nm, with minimal coupling to two blue-shifted modes. When the perturbations are moved to the right side of the bar, we see almost identical coupling to the broader mode, but much more efficient coupling to one of the blue-shifted modes. This provides an avenue for multiplexing of resonances within a metasurface element with greater flexibility than ring resonators, whose free

spectral range is largely controlled by the mode index and resonator size. Quality factors spanning 400 to 1500 are observed in this phase gradient geometry.

8. Mode symmetry and beamsplitting metasurface design.

Fig. 4 in the main text shows the generality of our phase gradient scheme beyond that of beamsteering. Here, we utilize two phase "pixels" which impart a different delay on the incident wave. In the design, one element is represented by a region with no silicon, while the other element consists of two coupled silicon nano-bars. To visualize the effect resulting from this structure, in supplementary Fig. S14 we compare the simulated electric field for transmission through the bare substrate with that of the double-bar, analogous to supplementary Fig. S3. As seen, the two fields are π out of phase with each other. This phase difference means that scattering from the periodic metasurface will be cancelled out in the 0^{th} order direction. The phase buildup equally suits propagation in the $+1^{st}$ and -1^{st} orders, meaning that an equal amount of the incident light will be sent into these two directions.

Unlike the beam steering metasurfaces, the small separation between the nano-bars here causes the modes to hybridise and energetically split. Supplementary Fig. S15 shows the guided mode dispersion for the beam splitting metasurface, as well as representative electric field intensity maps with polarization arrows. We have included the first 6 modes that exist in the wavelength range of interest, with only 4 crossing the grating momentum given the perturbation used in the main text (period 690 nm, dashed line). The 4 relevant modes appear in even and odd pairs (bonding and anti-bonding) with 2 different polarizations (i.e. x or z-polarized using the coordinate scheme of the main text). The small frequency splitting between these modes means that frequency multiplexing can be achieved rather easily in a narrow spectral range with

individual metasurface elements. Further, modal symmetry can be exploited as an additional tuning knob in high-Q metasurface design.

In addition to the spectral information presented in Fig. 4 of the main text, we performed Fourier plane spectroscopy of the beamsplitting metasurfaces, shown in Fig. S16. We clearly see balanced diffraction into the $+1^{st}$ and -1^{st} diffraction orders over a 50 nm wavelength range. Additionally, the two high-quality factor resonances shown in the main text are most visible in the self-normalized 0^{th} order scattering, which appear at 1389 nm and 1398 nm, respectively. We also varied the perturbation depth for the beamsplitting metasurface in 20 nm increments, spanning 30 nm to 70 nm. The spectra for these samples are presented in Fig S17, revealing two GMRs. As the perturbation depth is increased, the two modes begin to coalesce and eventually form a single lower quality factor resonance. In all cases, efficient beamsplitting is observed across the entire spectral range, while the 0^{th} order diffraction is efficiently suppressed. Thus, the design principles we present in the main text are generalizable to any transfer function of interest.

While four guided solutions exist for the beamsplitting metasurface, upon the addition of a periodic perturbation, only two of these solutions form resonances in Fig. S17. This can be understood by looking at the mode emission symmetry. Supplementary Fig. S18 shows the eigenmode electric fields for three resonances, color coded to match the dispersion curves in supplementary Fig. S15. The left and center panels correspond to the GMRs measured in Fig. 4b of the main text. The right panel, on the other hand, is an example of an eigenmode of the beam splitting metasurface that cannot be excited by a normally incident plane wave with an electric field polarised within the diffraction plane. The lack of excitability comes from the fact that the

plane wave is antisymmetric with respect to the central vertical axis, whereas the GMR is symmetric.

9. Optical Characterization Setup and beamsplitting metasurface parameter variation

Fig. S19 shows the optical setup for our measurements. Our metasurfaces were designed such that spectral and spatial information can be generated simultaneously. Projecting the diffraction axis in one direction of our CCD detector and projecting the spectral information on the other using a diffraction grating in our grating spectrometer (Princeton Instruments), we can simultaneously map the transfer function and spectral information using a white light laser (NKT). Weakly focusing our laser onto the metasurface, we collect the diffracted light through a 0.42 NA objective and focus the resultant spectra onto the camera. The weak focusing and polarizing optics are placed in a cage structure with our sample and put on a vertical rotation mount designed to be eucentric about the focal point of the objective, such that angle-resolved microscopy and spectroscopy measurements can be done. Further, we place a lens on a flip mount which is focused on the back focal plane of the objective. In doing so, we can project the momentum space image of the transfer function onto the camera.

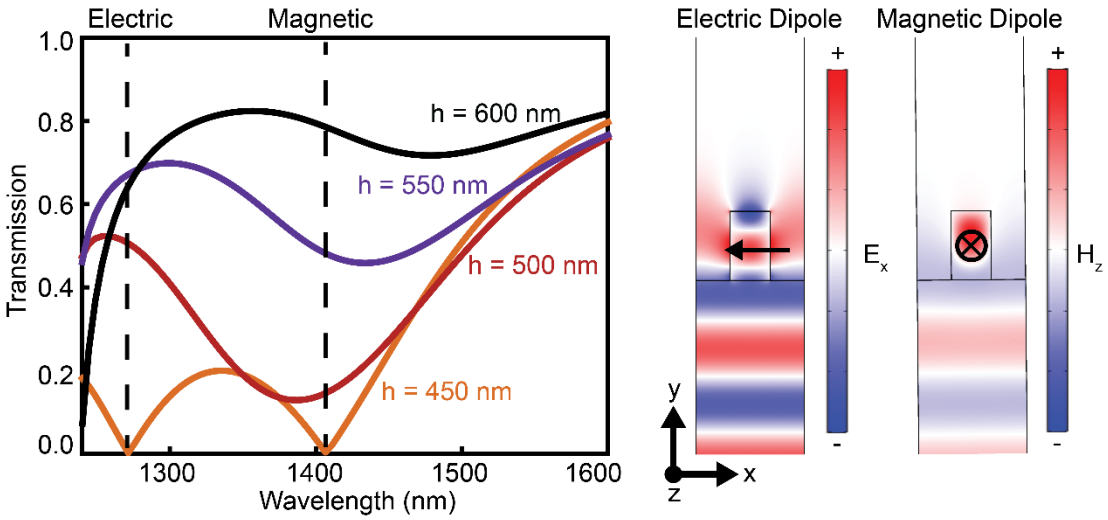

Fig. S1. Kerker-like condition in silicon nanobars. (left) Transmission amplitude as a function of nanobar height from 450 nm to 600 nm. At 450 nm, two resonances appear at 1270 and 1400 nm, while the transmission increases markedly as the nanobar height reaches 600 nm. (right) Electric and magnetic field plots for the modes at 1270 and 1400 nm, respectively. These field plots show that the resonances are electric and magnetic dipole-like in character.

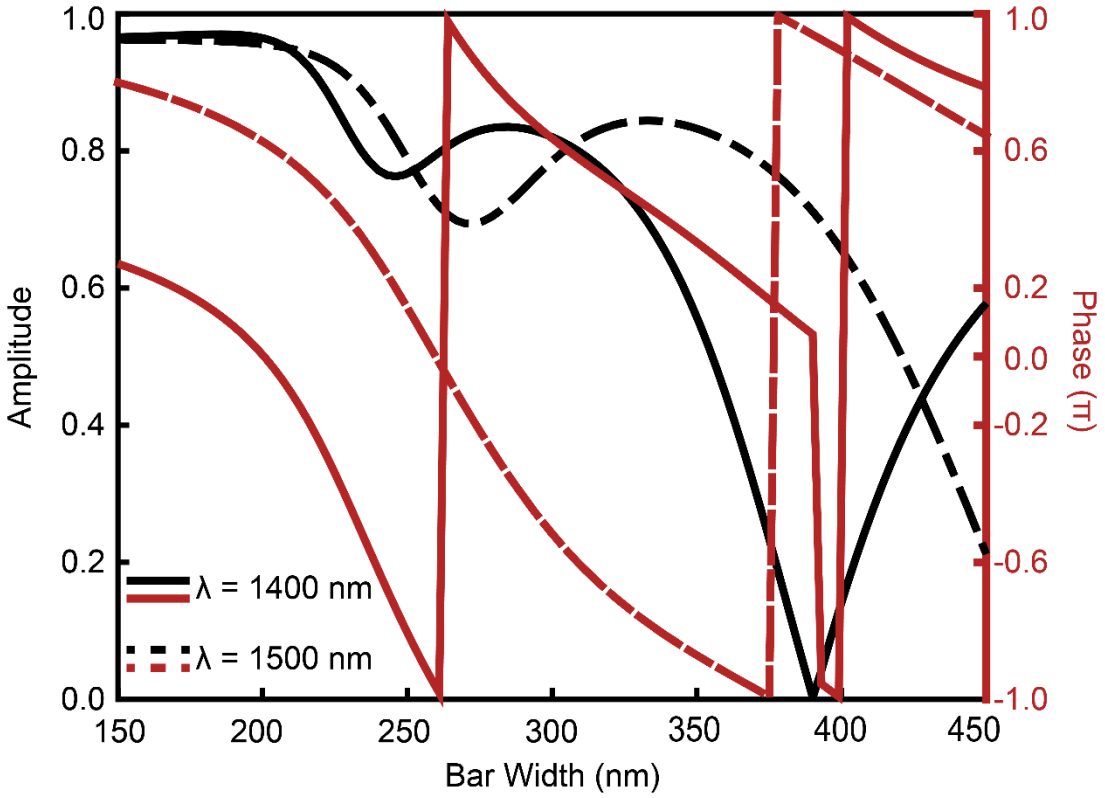

Fig. S2. Parameter sweep of beamsteering metasurfaces. Amplitude (black) and phase (red) response for Silicon metasurface elements used in the main text. Solid line indicates response at 1500 nm, while dashed line indicates response at 1400 nm. The amplitude never drops below 40% while the phase curves show a 2π phase variation, indicating the broad overlap of the electric and magnetic dipole Mie resonances

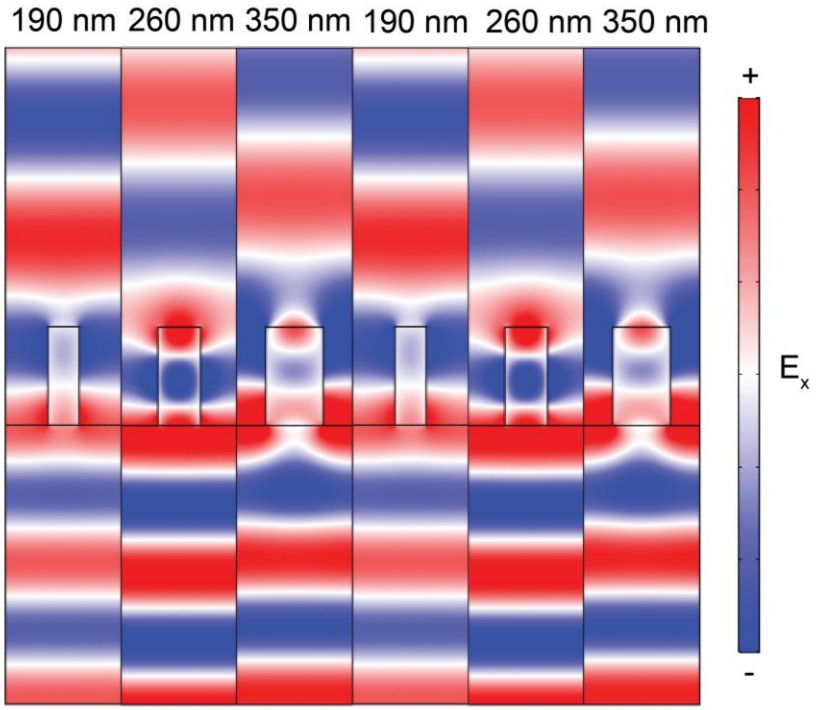

Fig. S3. Visualizing the phase gradient construction. Three metasurface elements are periodically arranged spatially, with the transmitted amplitude shown. Each bar is simulated with periodic boundary conditions giving rise to the beamsteering response. This can be seen by tracing a line of constant phase in the transmitted light; as seen, light is preferentially sent to the $+1^{st}$ order, at an angle specified by the metasurface dimensions.

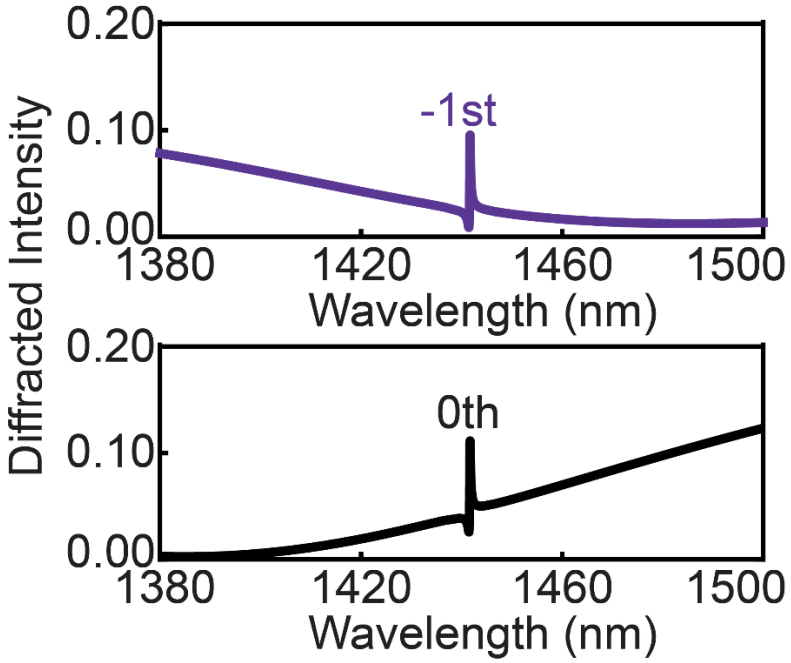

Fig. S4. Simulated transmittance for the 0th (black) and -1st (purple) diffraction orders from Fig. 1d of main text, plotted separately to see the lineshape. As seen, a similar lineshape exists for both orders, where an increase in transmittance is observed on resonance.

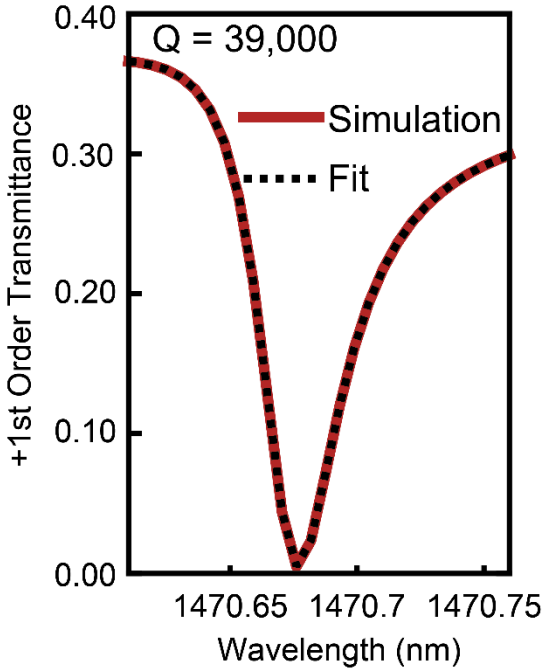

Fig. S5. Transmitted intensity for higher-Q structure. Simulated intensity (solid line) and fit (dashed line) for the design in Fig. 2 of main text but with a notch depth of 50 nm. The fit indicates a quality factor of approximately 39,000

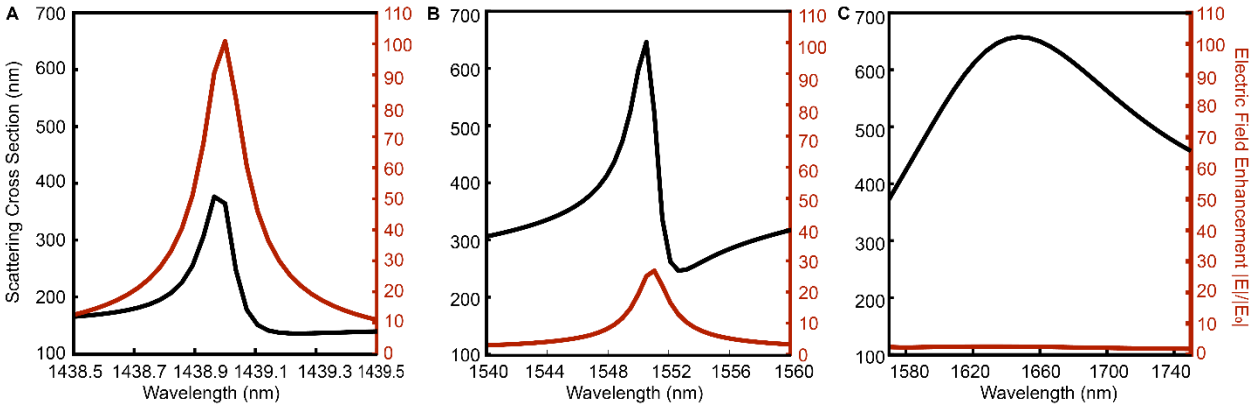

Fig S6. Guided mode resonance in isolated nanobar. Simulated scattering cross section (black, left axis) and resonant field enhancement (red, right axis) for isolated periodically perturbed nanoantenna with dimensions matching the largest element in Fig. 1 of the main text. All axes are equally scaled for direct comparison. A and B) reveal that even in an isolated nanoantenna the subtle periodic perturbation can generate high Q guided mode resonances. C) shows the low Q Mie resonance originating from the cross-sectional dimensions of the bar. While the three modes exhibit drastically different field amplifications, their peak scattering cross sections are roughly the same, which justifies treating Mie and guided mode resonances on the same footing when analyzing the farfield response of our metasurfaces.

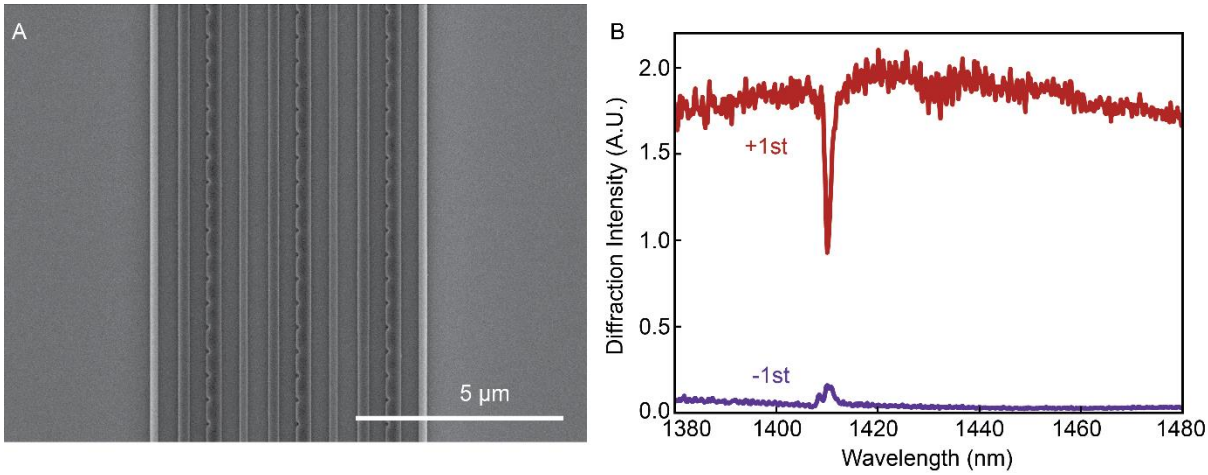

Fig S7. Scaling down metasurface dimensions does not impact high-Q resonances. A) SEM image of fabricated 10 bar device, with lateral dimension approximately 7 µm. B) Spectra of diffraction into $+1^{st}$ and -1^{st} diffraction orders, showing a high-Q resonance. Using identical illumination conditions as in the main text, we are unable to report the 0^{th} order due to the beam spot (~200 µm) being much larger than the finite size along the phase gradient direction.

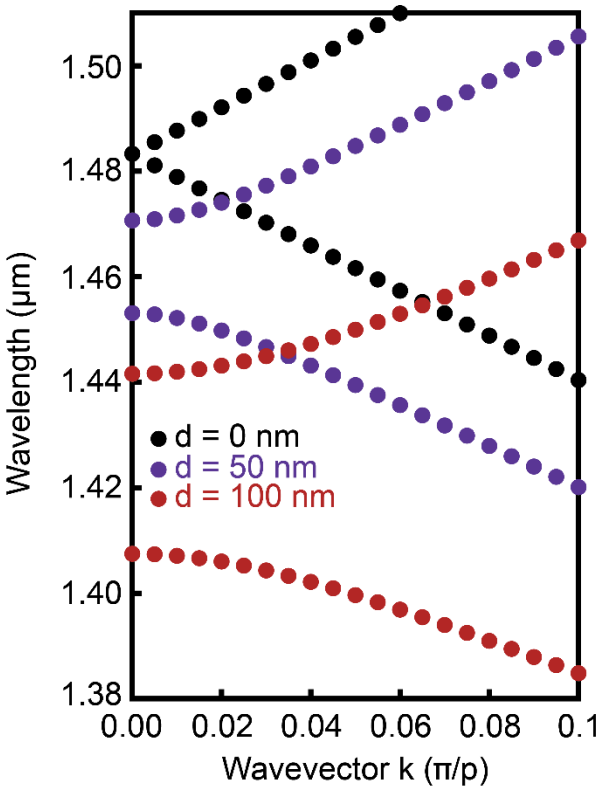

Fig. S8. Simulated guided mode dispersion in periodically perturbed nanoantenna as a function of perturbation depth. The notched bar geometry here corresponds to the notched bar in Fig.1 and Fig.2a-e of the main text.

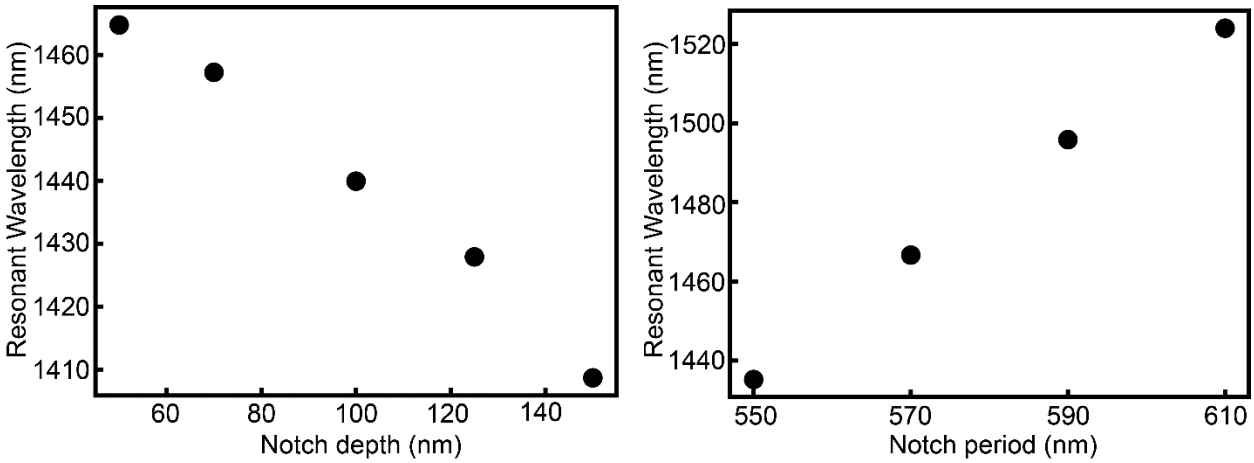

Fig. S9. Fitted values for the resonant wavelengths using the data reported in Fig.2 of main text.

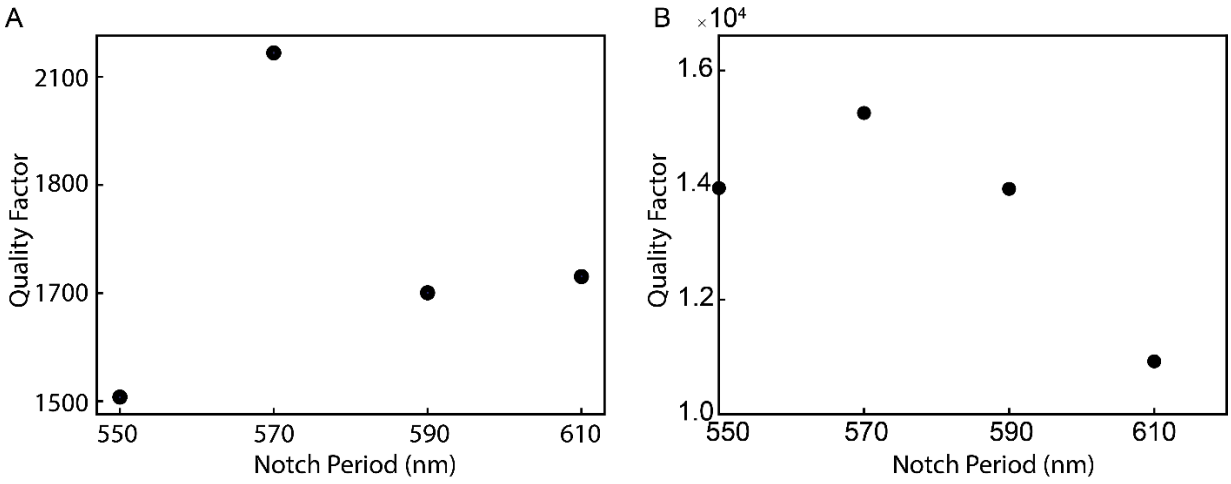

Fig. S10. Fitted values for the Q factors using the data reported in Fig.2e of main text. A) experimental data, B) simulated data.

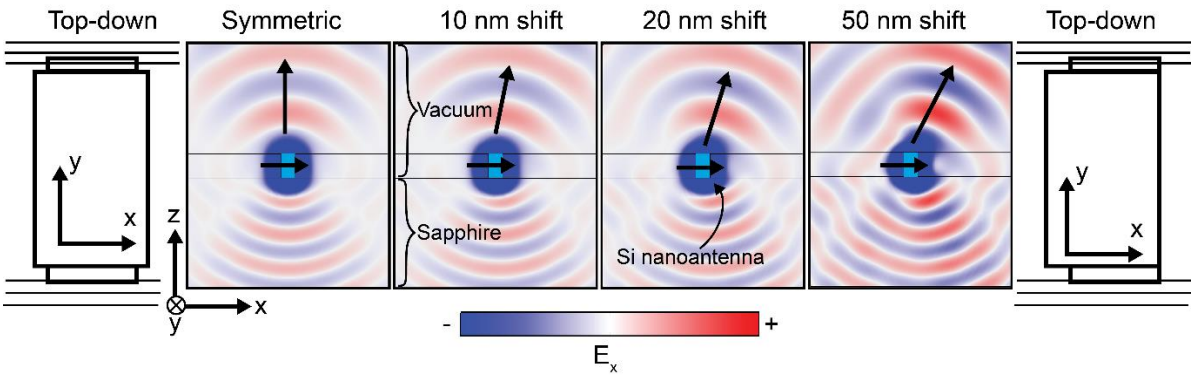

Fig. S11. Eigenmode emission patterns for in-plane polarised electric dipole GMR as a function of notch symmetry for the largest bar in our beamsteering metasurfaces. The narrowed region formed by the notch is being shifted increasingly to the right. The structural shift directs the emission intensity slightly towards the right.

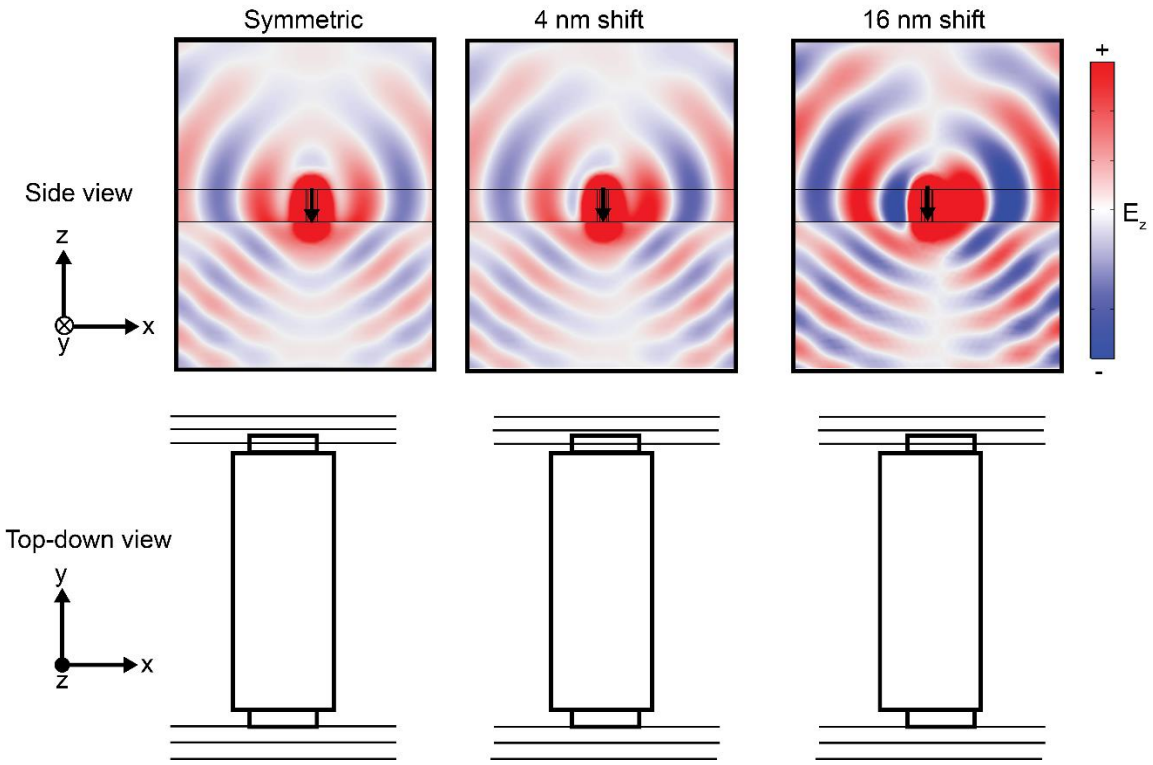

Fig. S12. Eigenmode emission patterns for vertically polarised electric dipole GMR as a function of notch symmetry in the thinnest bar in Fig. 3 of main text. As shown via the top down images to the left of each simulation, the narrowed region formed by the notch is being shifted to the right by 4 nm (center) and 16 nm (right). The structural shift causes a phase delay for the wave emitted to the right compared to the left. The bar geometry of the middle plot (4 nm shift) is used in Fig. 3 of the main text.

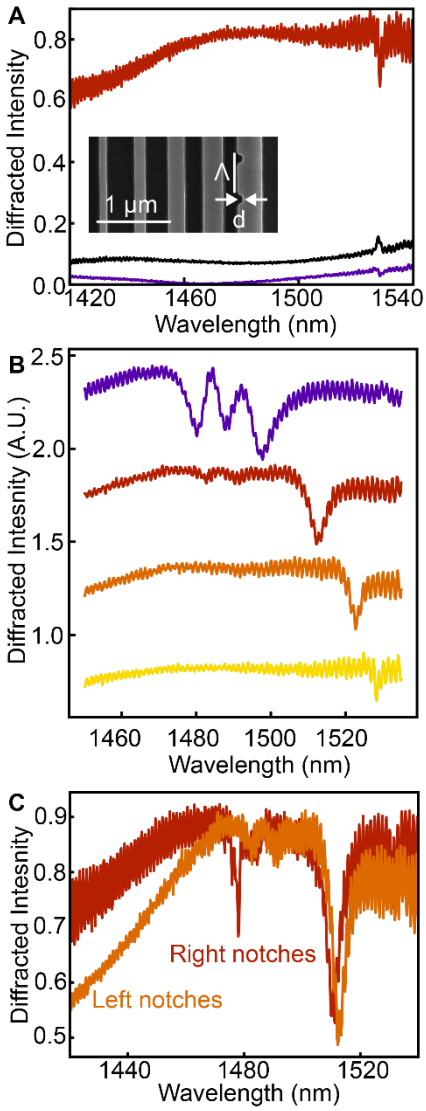

Fig. S13. Efficient beamsteering and mode multiplexing. A) Beamsteering spectrum for samples that deflect light to 36 degrees. Perturbation pitch 550 nm, depth 30 nm. B) Diffracted spectra for samples with varying depth, showing the same redshift and increasing quality factor with decreasing perturbation. For d = 50-100 nm, each curve has been shifted vertically by 0.5 relative to the previous curve. C) Different high-Q modes excited when perturbation is on the left or right side of the largest bar.

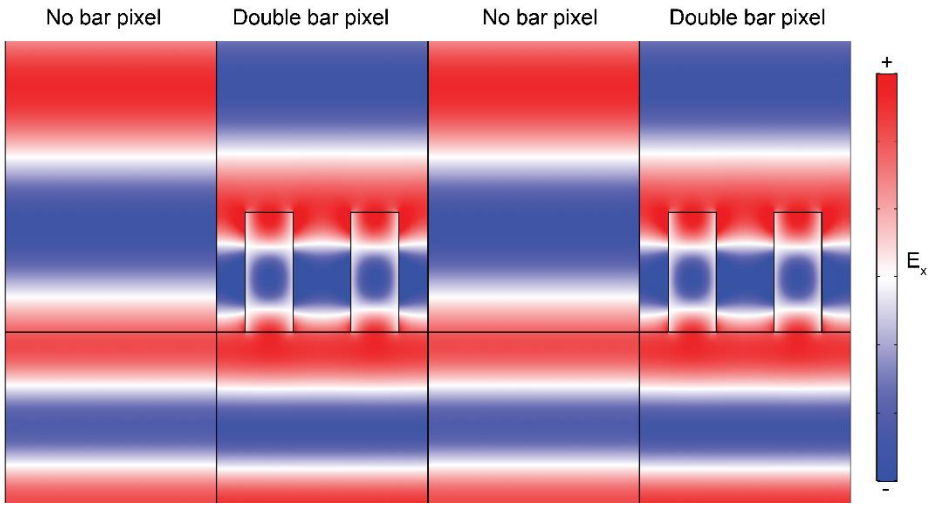

Fig. S14. Visualizing binary phase grating construction. Beam splitting from combination of blank phase pixel and double bar phase pixel, exhibiting π difference in their transmitted phase delay. Two unit cells are shown.

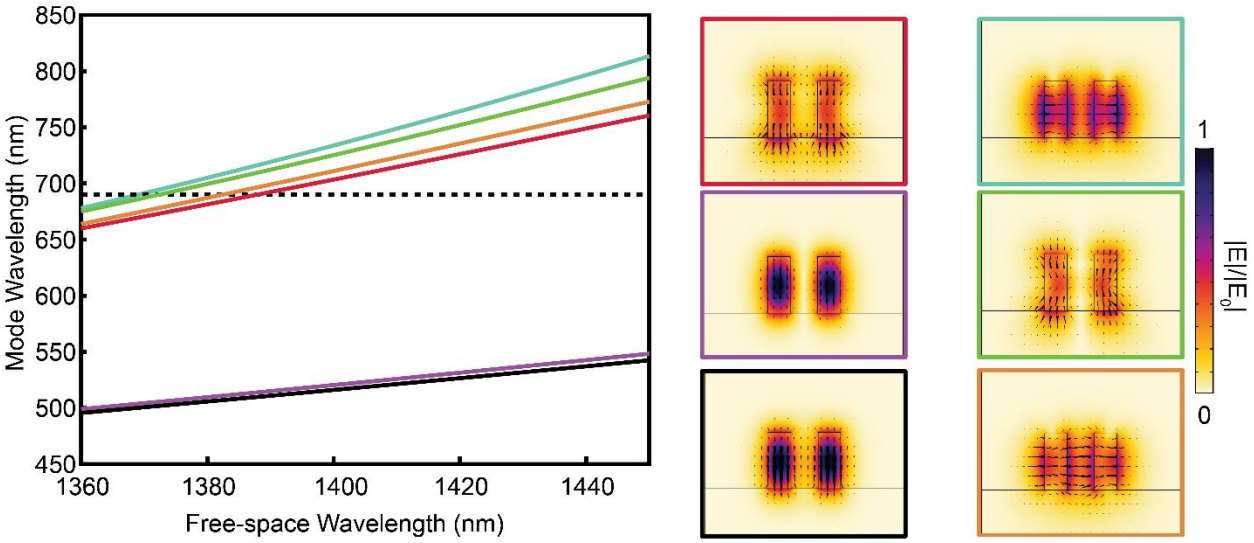

Fig. S15. Guided modes of beam splitting metasurface. Curves are colour coded to match the mode profiles on the right. Dotted line represents notch period used in Fig.4 of main text.

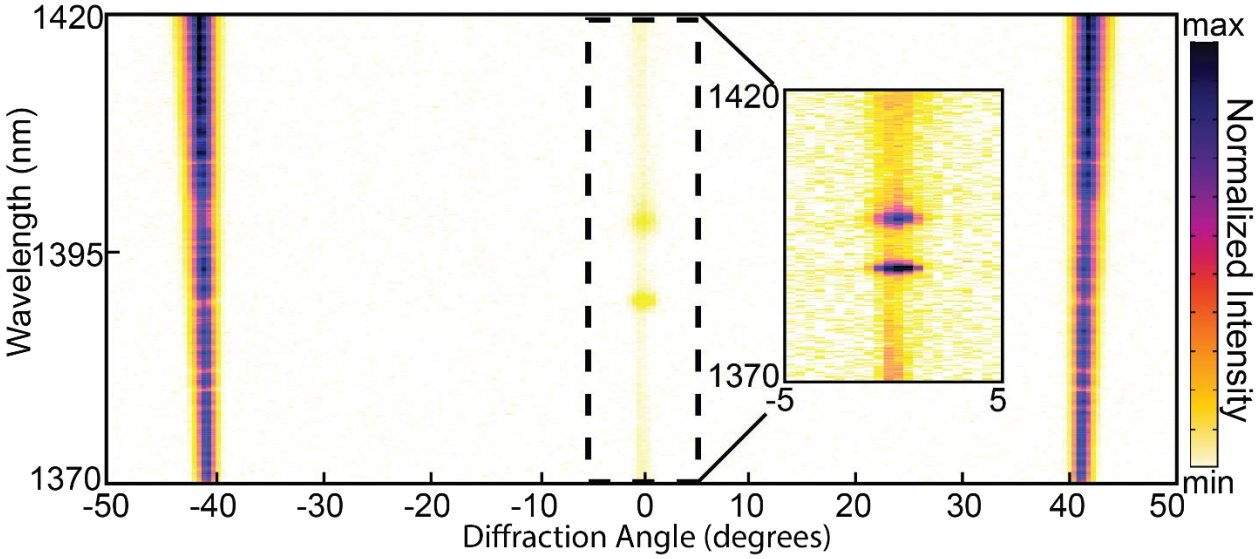

Fig. S16. Angle-resolved spectra of beamsplitting metasurface in Fig. 4 of main text. Minimal intensity is transmitted in the 0th order, while equally intensity is observed for the +/- 1st diffraction orders (~+/-40 degrees). The inset shows the 0th order diffraction self-normalized, highlighting the increased intensity in two small bands near 1389 and 1398 nm. These correspond to the resonances in the beam splitting spectrum.

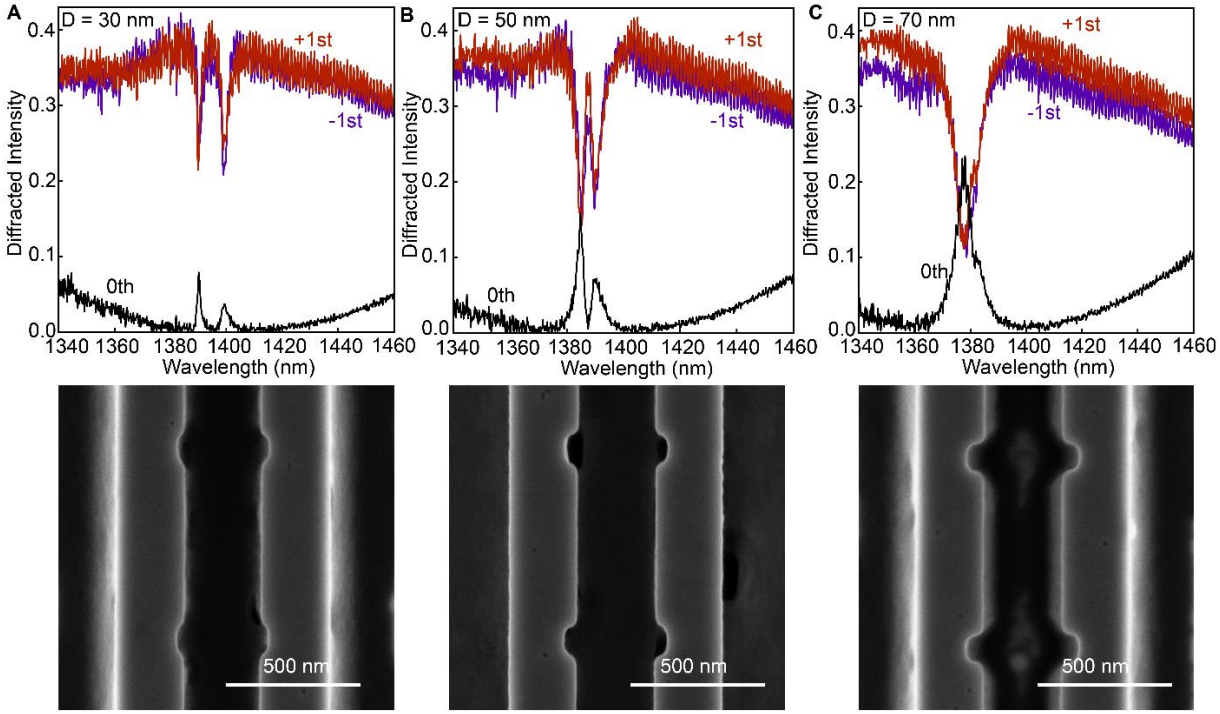

Fig. S17. Parameter sweep of beamsplitting metasurface. Diffraction intensity (y-axis) as a function of wavelength (x-axis) for 3 separate beamsplitting metasurfaces. The inset to the first plot shows a unit cell of the geometry, with a perturbation depth of 30 nm (left), 50 nm (middle), and 70 nm (right). Equal intensity in the $+1^{st}$ and -1^{st} diffracted orders are seen, while a minimum in the 0^{th} order is seen. The 70 nm notch depth only exhibits one low-Q resonant wavelength. Corresponding SEM is shown below each spectrum.

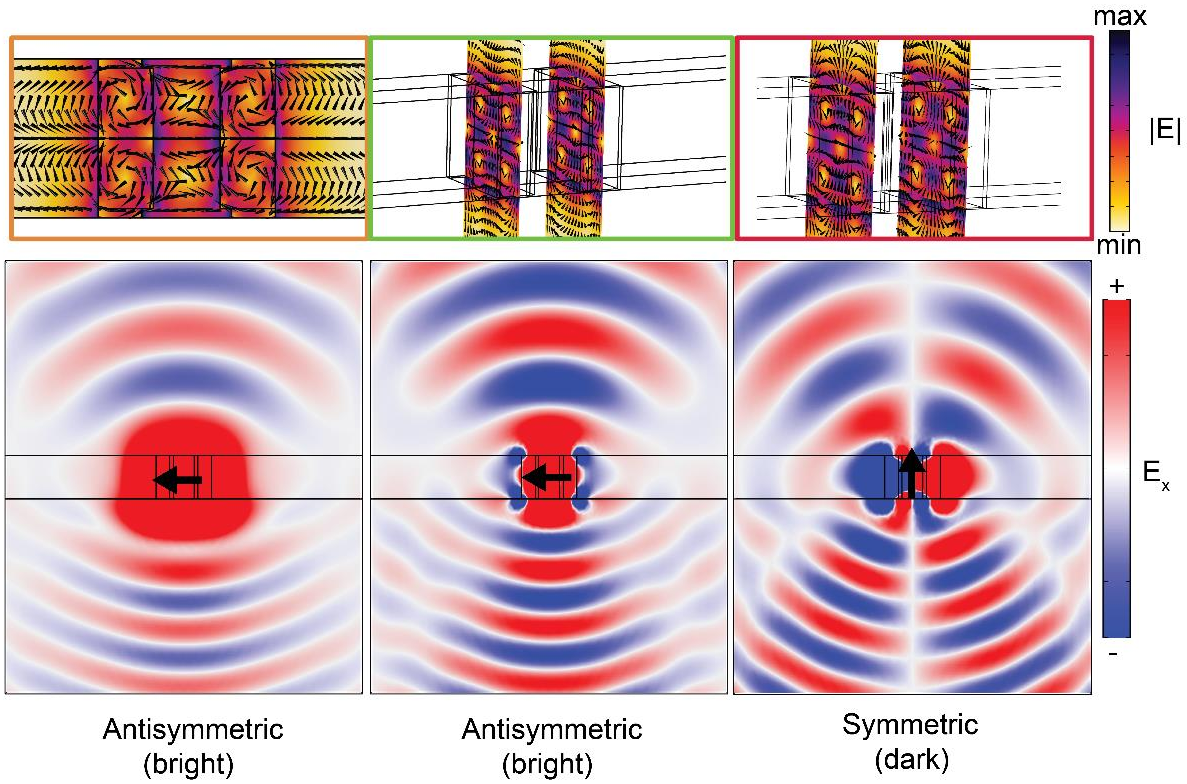

Fig. S18. Eigenmodes of the notched double bar nanoantenna. Eigenmodes of the notched double bar nanoantenna. Simulated near-field distributions (top row) and emission patterns (bottom row) for three guided mode resonances, colour coded to match the guided modes in Fig. S15.

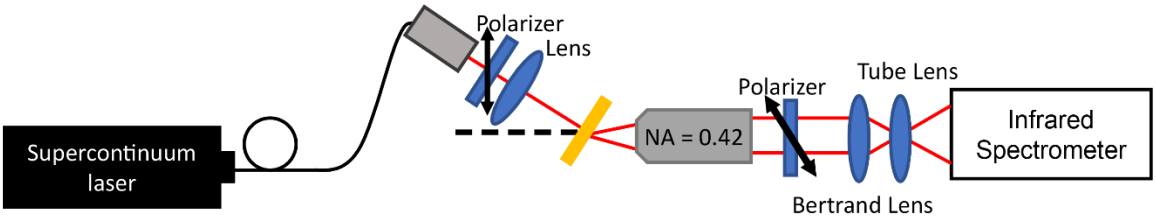

Fig. S19. Angle-resolved microscope for spectroscopic measurements. A broadband laser (NKT supercontinuum) is polarized and focused onto the metasurface. The laser, focusing optics, and metasurface are mounted on a rotating cage structure. The metasurface is mounted at the eucentric position, which lies in the focal plane of the 0.42 NA objective. Collected light travels through polarizers and lenses to be projected onto the CCD of a spectrometer.